HOKKAIDO UNIVERSITY

Title	A facile solution combustion synthesis of nanosized amorphous iron oxide incorporated in a carbon matrix for use as a high-performance lithium ion battery anode material
Author(s)	Zhu, Chunyu; Saito, Genki; Akiyama, Tomohiro
Citation	Journal of Alloys and Compounds, 633, 424-429 https://doi.org/10.1016/j.jallcom.2015.02.043
Issue Date	2015-06-05
Doc URL	https://hdl.handle.net/2115/58573
Type	journal article
File Information	manu-14-final.pdf

Hokkaido University Collection of Scholarly and Academic Papers : HUSCAP

A facile solution combustion synthesis of nanosized amorphous iron oxide incorporated in a carbon matrix for use as a high-performance lithium ion battery anode material

Chunyu Zhu [a]*, Genki Saito [a], Tomohiro Akiyama [a]

[a]Center for Advanced Research of Energy & Materials, Hokkaido University, Sapporo 060-8628, Japan

*Corresponding author: Tel.: +81-11-706-6842; Fax: +81-11-726-0731.
E-mail address: chunyu6zhu@gmail.com or chunyu6zhu@eng.hokudai.ac.jp (Chunyu Zhu)

Abstract

An amorphous iron oxide-carbon composite has been fabricated through an effective, inexpensive, and scalable method employing solution combustion synthesis. Amorphous iron oxide nanoparticles with diameters of about 5 nm were synthesized and uniformly embedded in a dense carbon matrix. The synthesized composite exhibits enhanced cyclability and rate capability, showing a high reversible capacity of 687 mAh g^{-1} after 200 discharge/charge cycles at a current rate of 0.5 A g^{-1}, compared to the 400 mAh g^{-1} observed for Fe_2O_3 nanoparticles. This enhanced performance was retained despite more demanding conditions, delivering a high capacity of about 525 mAh g^{-1} and a nearly perfect coulombic efficiency even after 400 cycles at 1 A g^{-1}. The easy production and superior electrochemical properties of this composite suggest that it is a promising material for use as an anode material in high performance lithium ion batteries.

Keywords: iron oxides, lithium ion battery, anode material, nanoparticle, composite

Introduction

Lithium ion batteries (LIBs) are one of the most promising power sources for portable electronic devices, electric vehicles and hybrid electric vehicles due to their high energy density and long life.[1, 2] As a result, significant research has been completed to develop new anode and cathode materials with higher capacities to replace the conventional graphite/$LiCoO_2$ systems. Transition metal oxides, including those of iron[3-5], cobalt[6-8], manganese[9-12], nickel[13, 14], and copper[15-17], have attracted particular attention as anode replacements because of their higher theoretical capacities when compared to commercial graphite and the potential to increase their rate capability by more finely controlling their nanostructure.[18, 19] Iron oxides are particularly attractive in this regard given their high capacities, low cost, environmental friendliness, and the natural abundance of iron. However, their practical application has been hindered by poor cycling performance and low rate capability owing to low electrical conductivity and significant distortion during Li insertion/extraction.[2, 20] Nanostructural control and coating or compositing with carbon materials have shown some success in overcoming this issue.

Nanostructures with increased surface area improve contact between the solid and the electrolyte, shorten the route for lithium diffusion, and minimize the effects of volume change.[20, 21] Various iron oxide nanostructures, including nanoparticles[22, 23], nanorods[24, 25], yolk-shell structures[26], and hollow structures[27, 28], have been developed and show improved electrochemical properties. However, an increase in surface area increases the chance of side reactions, yielding low coulombic efficiency for lithium deintercalation/intercalation and poor cycling performance as a result. Conductive carbon materials are especially promising coating and compositing agents for iron oxides given that they can increase electronic conductivity and enhance lithium diffusion. In particular, compositing can effectively buffer volume change and prevent the nanostructures from being pulverized during repeated lithiation/delithiation.[18, 20] Many reports have been engaged with the production and application of iron oxide-carbon nano-composites for the anode of LIBs.[29-32] However, the ease with which nanomaterials aggregate and their high surface area makes coating difficult, limiting the potential for large-scale application. This increased surface area also results in low coulombic efficiency due to the formation of a large, unstable solid electrolyte interface

(SEI) during lithiation/delithiation. Embedding nanostructured iron oxides in microscale carbon materials with limited surface area is one potential way to overcome these limitations. However, it remains a great challenge to fabricate iron oxide-carbon anodes by a facile and scalable method.

Solution combustion synthesis (SCS) is a highly exothermic and self-sustaining reaction process by heating a solution mixture of aqueous metal nitrates and organic fuels. A variety of functional oxides, such as perovskite oxide catalysts[33] and cathode oxide materials[34, 35] for LIBs has been synthesized by this method. This approach offers several benefits, such as (1) the utilization of an exothermic reaction requiring no additional energy during the combustion process, (2) larger surface areas of nanosized or porous products, (3) homogeneous doping of trace amounts of various elements in a single step. By controlling the combustion reaction conditions to avoid the complete combustion of the carbonaceous material, the remaining carbon material and metal oxides can form composites for advanced LIB anode materials. This can be achieved by (1) adding excess amount of fuel and (2) lowering the combustion temperature to avoid the combustion of carbon.

Herein, we report a simple method to directly incorporate nanosized amorphous iron oxides into a dense carbon matrix through a facile solution combustion synthesis (SCS) that is suitable for large-scale application. The resulting composite material, FeO_x/C, exhibits high discharge/charge capacities, superior cycling performance, and excellent rate capability.

Experimental section

SCS of FeO_x/C composite: Fig. 1 provides a schematic diagram for the SCS of the FeO_x/C precursor as modified from references[33, 34, 36]. Commercially available $Fe(NO_3)_3$▪$9H_2O$ (20 mmol) and glycine (140 mmol) were dissolved and mixed in distilled water. After complete dissolution, the excess water was evaporated by heating to 80-100 ^oC under stirring until a viscous gel was formed. Next, the gel was placed in an alumina crucible, transferred to a locally produced SCS apparatus, and introduced to a heater at 400 ^oC.[33] Upon reaching 200 ^oC, the gel quickly combusted, releasing a large amount of gases; at this point, power to the heater was immediately turned off to avoid burning the precursor further. The post-SCS material was then heated from 500 ^oC to 700 ^oC for over 2 h under Ar to obtain the desired composites. A separate sample of precursor was heated in air to obtain the corresponding Fe oxide nanoparticles for comparison.

Material characterization: Powder X-ray diffraction (XRD, Rigaku Miniflex) was used to analyze the phase composition. Scanning electron microscopy (SEM, JEOL, JSM-7400F) was combined with X-ray energy dispersive spectrometry (EDS); these were used to analyze sample morphology and elemental composition, respectively. Transmission electron microscopy (TEM, JEM-2010F, 200 kV) was employed for a detailed analysis of the composite product. Thermogravimetric (TG, Mettler Toledo) analysis was used to determine reaction behavior during heat treatment and carbon content of the composite.

Electrochemical measurements: Electrochemical measurements were performed using a two-electrode union-joint cell based on a modified Swagelok-type design. The working electrode was constructed by preparing a slurry of the active material, conductive carbon (acetylene black), and a polyvinylidene fluoride (PVDF) binder, in a weight ratio of 70:20:10, in N-methyl-2-pyrrolidone (NMP) solvent; this slurry was then coated onto a Cu foil current collector. The coated electrodes were dried under vacuum at 110 ^oC for 12 h and cut into 14 mm disks with mass load of about 2-3 mg.

A 1 mol L^{-1} solution of $LiPF_6$ dissolved in a 50:50 (v/v) mixture of ethylene carbonate (EC) and dimethyl carbonate (DMC) was used as the electrolyte, while a Celgard glass fiber was used as the separator. Cell assembly was carried out in an Ar-filled glove box. In addition, a lithium disk was used as both the counter and reference electrode. A battery tester (Arbin)

was employed for galvanostatic discharge/charge measurements, which were completed in a voltage window of 0.01 and 3.0 V versus Li/Li^+ and at a constant temperature of 25 ºC. Cyclic voltammetry (CV) measurements were carried out using a potentiostat/galvanostat apparatus (Autolab, PGSTAT128N) set to a potential scanning rate of 0.1 mV s^{-1} and a voltage range of 0.01-3.0 V.

Results and discussion

Fig. 2 shows XRD patterns for samples obtained at different treatment stages. The patterns for samples obtained immediately after SCS (Fig. 2a) and after 2 h of a 500 ^{o}C heat treatment unde Ar (Fig. 1b) indicate an amorphous pattern for both. On the other hand, the sample treated for 2 h under air showed XRD patterns which indicate a single phase of α-Fe_2O_3 (JCPDS no. 33-0664). However, samples calcined at 600 ^{o}C or 700 ^{o}C for 2 h under Ar contain metallic α-Fe (JCPDS no. 65-4899), demosnstrated by the typical peak (110) at about 44.7 ^{o}.

TG analysis (Fig. 3-(1)) was used to determine the reaction behavior of the various samples. The post-SCS samples (Fig. 3-(1)-a) lost weight up until 450 ^{o}C under air, indicating the complete combustion of carbonaceous materials and the formation of temperature-stable Fe_2O_3. Unsurprisingly, the sample treated under Ar (Fig. 3-(1)-b) avoided carbon oxidation; while weight loss below 540 ^{o}C was due to decomposition of unstable carbonaceous materials, weight loss above that temperatrue seemingly resulted from the reduction of iron oxide to metallic iron by carbon, as shown in the following formula:

$$FeO_x + C \rightarrow Fe + CO_2/CO \qquad (1)$$

The formation of metallic iron was also confirmed by the presence of the corresponding peak in the XRD spectrum. Finally, the TG curve for the calcined composite in air (Fig. 3-(1)-c) showed a weight loss from 150 ^{o}C to 500 ^{o}C corresponding mainly to carbon oxidation; assumming that the amorphous iron oxide can be represented with the formula Fe_2O_3, the calculated carbon content is about 51%.

The morphologies and microstructures of the samples were further investigated using SEM and TEM. Fig. 4 indicate that FeO_x/C has a complex structure in the bulk form with a smooth surface in 1-10 μm range, while the Fe_2O_3 sample is composed of nanoparticles of about 100 nm in diameter. Meanwhile, magnified bright-field TEM image in Fig. 5 indicates that iron oxide nanoparticles with a diameter of about 5 nm were embedded in the bulk carbon matrix.

EDS was used to probe the chemical composition of FeO_x/C; the corresponding data is shown in Fig. 4-c. It shows that the composite consists of carbon, nitrogen, iron, and oxygen. The presence of oxygen can mainly attributed to iron oxide, as well as a small amount of adsorbed O_2 and CO_2. Meanwhile, the nitrogen primarily derives from residual glycine and trace nitric ions. Mass spectrometry (as shown in Fig. 3-(2)) of the gas released during TG analysis detected nitrogen oxide, further corroborating these results. It has been reported that nigrogen-doping can enhance the electronic conductivity of carbon-based materials, therefore improving electrochemical performance.[37, 38]

With physical testing complete, the FeO_x/C composite was then subjected to electrochemical testing, starting with galvanostatic discharge/charge at a current density of 500 mA g^{-1}; the pure Fe_2O_3 nanoparticles were measured under the same conditions for the sake of comparison. Fig. 6 shows capacity and coulombic efficiency data with respect to cycling number, while Fig. 7 presents the corresponding discharge and charge profiles for multiple cycles. The initial discharge/charge capacities are 1211.6/803.9 mAh g^{-1} for FeO_x/C and 1373.4/1013.8 mAh g^{-1} for Fe_2O_3, respectively, with corresponding initial coulombic efficiencies of 66.35% and 73.82%, respectively. The discharge capacity of the first cycle often exceeds the theoretical capacity of materials being tested due to irreversible electrochemical reactions, such as the formation of an SEI layer and the decomposition of the electrolyte.[39-42] Following the first cycle, the discharge capacity of FeO_x/C reached 700.6 mAh g^{-1}, then slowly and continuously decreased to 573.6 mAh g^{-1} by the 30th cycle; at this point, the capacity slowly increased, reaching 687.4 mAh g^{-1} by the 200th cycle. Additionally, coulombic efficiency was maintained throughout, staying close to 100% even through the 20th cycle. Meanwhile, Fe_2O_3 showed a substantial decrease in capacity, dropping from 1046.0 mAh g^{-1} to 389.1 mAh g^{-1} by the 63rd cycle and stabilizing at about 400 mAh g^{-1} by the 200th cycle. Furthermore, Fe_2O_3 efficiency slowly increased from about 91%, stabilizing at about 98% by the 50th cycle.

The initial discharge and charge voltage profiles of FeO_x/C and Fe_2O_3 are quite different, as shown in Fig. 7. The initial discharge curve for Fe_2O_3 shows three voltage plateaus at approximately 1.6, 1.0, and 0.85 V, all of which can be attributed to the following multi-step lithiation reaction: [41, 42]

$$Fe_2O_3 + xLi^+ + xe^- \rightarrow \alpha\text{-}Li_xFe_2O_3 \quad (2)$$

$$\alpha\text{-}Li_xFe_2O_3 + (2\text{-}x)Li^+ + (2\text{-}x)e^- \rightarrow Li_2Fe_2O_3 \text{ (cubic)} \quad (3)$$

$$Li_2Fe_2O_3 + 4Li^+ + 4e^- \leftrightarrow 2Fe^0 + 3Li_2O \quad (4)$$

In the initial, short plateau at 1.6 V, a small amount of lithium is inserted into the crystal structure of Fe_2O_3, while its structure is kept. Meanwhile, the second plateau at 1.0 V corresponds to additional lithium intercalation and the subsequent conversion of hexagonal α-$Li_xFe_2O_3$ to cubic $Li_2Fe_2O_3$. The final, extended plateau at 0.85 V corresponds to the complete reduction of iron from Fe^{2+} to Fe^0 and accompanying electrolyte decomposition. Any additional activity below 0.85 V is due to the formation of an SEI layer and electrolyte decomposition, causing the irreversible portion of the discharge capacity;[39-42] reverse delithiation between 1.2 and 2.2 V is present in the opposing charge process.

The discharge/charge curves for FeO_x/C show no obvious plateaus; this dramatic difference between the two samples is likely the result of significant carbon intercalation. Note that, in the first discharge process, the potential of the cell quickly dropped to 1.2 V; at this point, lithium intercalation proceeded slowly, resulting in an initial lithium storage capacity of 1211.6 mAh g^{-1}.

CV tests were employed to further investigate electrochemical performance, specifically focusing on the oxidation/reduction and phase transformation processes that occur at the electrodes. Fig. 8 shows the CV curves of FeO_x/C and Fe_2O_3. A substantial difference is visible between the first cycle and all subsequent one for Fe_2O_3 electrode. In the first cycle, cathodic peaks are visible at about 1.66, 0.93, and 0.64 V, corresponding to the lithiation processes represented in the first galvanostatic discharge profile. Note that the observed shift between the CV peak voltages and discharge plateau voltages result from the different scanning speeds. The reduction peak area drops significantly in the second cycle, suggesting an irreversible process. Likewise, similar anodic peaks are present at about 1.8 V

in the first four cycles of opposing delithiation process; these likely result from the oxidation of iron to iron oxide.

Meanwhile, FeO_x/C shows very weak anodic and cathodic peaks. CV data shows a broadened peak between 1.2-0.3 V in the first discharge, corresponding to the reduction of iron oxide to metallic iron and lithium oxide. Weak reduction peaks are found at about 0.9 V in the second discharge cycle. Meanwhile, similar anodic peaks are present in the initial four charge cycles at about 1.0 V, corresponding to the oxidation of iron to iron oxide. In addition, sharp cathodic peaks near 0.0 V are present in the initial four cycles, and likely result from the reaction of lithium with carbonaceous materials, including both the composite and conductive carbon. Overall, FeO_x/C shows lower cathodic and anodic potentials and shortened discharge/charge voltage hysteresis when compared to Fe_2O_3.

To further demonstrate the advantage of FeO_x/C for high-power LIB application, the rate performance was further tested under varying current densities as shown in Fig. 9. Current densities were progressively increased from 0.1 A g^{-1} to 3.0 A g^{-1} and then dropped back to 0.3 A g^{-1}. FeO_x/C exhibited excellent rate performance; after 80 cycles with an accompanying stepwise increase of 1.0 A g^{-1} in current density, the cell still showed reversible capacities of about 574, 524, 481, 441, and 400 mAh g^{-1} at current densities of 1.0, 1.5, 2.0, 2.5, and 3.0 A g^{-1}, respectively, demonstrating impressive performance at high rates. After cycling at increasing current rates of 3.0 A g^{-1} until 180th cycle, the capacity of the electrode could reach back to about 725 mAh g^{-1} at a current density of 0.3 A g^{-1}.

Discharge/charge performance was also evaluated at a constant rate of 1 A g^{-1} for 400 cycles, as shown in Fig. 10. Overall performances at 1 A g^{-1} and 0.5 A g^{-1} were very similar. Initial discharge and charge capacities were 1087.8 and 646.2 mAh g^{-1}, respectively, yielding a coulombic efficiency of 59.40%. The FeO_x/C discharge capacity decreased slowly and steadily after the second cycle, reaching 403.8 mAh g^{-1} by the 55th cycle, and then increasing slowly and stabilizing at about 525 mAh g^{-1} by the 300th cycle. Overall coulombic efficiency exceeded 99% for all cycles following the second.

The improved cycling retention and rate capability observed for FeO_x/C mainly result from the unique carbon matrix of the sample and the incorporation of nanosized oxides. The carbon matrix not only favors accelerated Li insertion/extration and electron transport, but

also works as a buffer to disperse nanosized particles and to alleviate the effect of volume changes during Li storage/release.

Conclusions

In summary, we have developed a facile SCS-based method for the synthesis of iron oxide-carbon composite that is effective, inexpensive, and scalable. Iron oxide nanoparticles with diameters of around 5 nm were uniformly embedded in the dense carbon matrix. The composite exhibited superior capacity retention and rate performance when used as an anode material in LIBs, showing a high reversible capacity of 687 mAh g^{-1} after 200 cycles at a current rate of 0.5 A g^{-1}. The performance of the material did not decrease significantly even after 400 cycles at 1 A g^{-1}, still delivering a high value of about 525 mAh g^{-1}. These results suggest that the developed synthetic method holds significant promise; it may even be possible to extend it to other metal oxides.

Acknowledgements

This work was partially supported by the Japan Society for Promotion of Science (JSPS).

References

1. W. W. Lee and J.-M. Lee, *Journal of Materials Chemistry A*, 2014, 2, 1589-1626.
2. M. V. Reddy, G. V. Subba Rao and B. V. R. Chowdari, *Chemical Reviews*, 2013, 113, 5364-5457.
3. S. Jia, T. Song, B. Zhao, Q. Zhai and Y. Gao, *Journal of Alloys and Compounds*, 2014, 617, 787-791.
4. H. Geng, Q. Zhou, J. Zheng and H. Gu, *RSC Advances*, 2014, 4, 6430-6434.
5. P. S. Veluri and S. Mitra, *RSC Advances*, 2013, 3, 15132-15138.
6. G. Chen, E. Fu, M. Zhou, Y. Xu, L. Fei, S. Deng, V. Chaitanya, Y. Wang and H. Luo, *Journal of Alloys and Compounds*, 2013, 578, 349-354.
7. L. Shen and C. Wang, *Electrochimica Acta*, 2014, 133, 16-22.
8. L. Zhuo, Y. Wu, J. Ming, L. Wang, Y. Yu, X. Zhang and F. Zhao, *Journal of Materials Chemistry A*, 2013, 1, 1141-1147.
9. G. Jian, Y. Xu, L.-C. Lai, C. Wang and M. R. Zachariah, *Journal of Materials Chemistry A*, 2014, 2, 4627-4632.
10. B. Liu, X. Hu, H. Xu, W. Luo, Y. Sun and Y. Huang, *Sci. Rep.*, 2014, 4.
11. J. Qin, Q. Zhang, Z. Cao, X. Li, C. Hu and B. Wei, *Nano Energy*, 2013, 2, 733-741.
12. X. Shen, Z. Ji, H. Miao, J. Yang and K. Chen, *Journal of Alloys and Compounds*, 2011, 509, 5672-5676.
13. V. Aravindan, P. Suresh Kumar, J. Sundaramurthy, W. C. Ling, S. Ramakrishna and S. Madhavi, *Journal of Power Sources*, 2013, 227, 284-290.
14. Y. Zhu, H. Guo, Y. Wu, C. Cao, S. Tao and Z. Wu, *Journal of Materials Chemistry A*, 2014, 2, 7904-7911.
15. L. Feng, Z. Xuan, Y. Bai, H. Zhao, L. Li, Y. Chen, X. Yang, C. Su, J. Guo and X. Chen, *Journal of Alloys and Compounds*, 2014, 600, 162-167.
16. S. Ko, J.-I. Lee, H. S. Yang, S. Park and U. Jeong, *Advanced Materials*, 2012, 24, 4451-4456.
17. Y. Xu, G. Jian, M. R. Zachariah and C. Wang, *Journal of Materials Chemistry A*, 2013, 1, 15486-15490.
18. M. Osiak, H. Geaney, E. Armstrong and C. O'Dwyer, *Journal of Materials Chemistry A*, 2014, 2, 9433-9460.
19. J. Jiang, Y. Li, J. Liu, X. Huang, C. Yuan and X. W. Lou, *Advanced Materials*, 2012, 24, 5166-5180.
20. L. Zhang, H. B. Wu and X. W. Lou, *Advanced Energy Materials*, 2014, 4, DOI: 10.1002/aenm.201300958.
21. S. Goriparti, E. Miele, F. De Angelis, E. Di Fabrizio, R. Proietti Zaccaria and C. Capiglia, *Journal of Power Sources*, 2014, 257, 421-443.
22. M. Du, C. Xu, J. Sun and L. Gao, *Journal of Materials Chemistry A*, 2013, 1, 7154-7158.
23. J.-K. Kim, L. Aguilera, F. Croce and J.-H. Ahn, *Journal of Materials Chemistry A*, 2014, 2, 3551-3556.
24. Z. Xiao, Y. Xia, Z. Ren, Z. Liu, G. Xu, C. Chao, X. Li, G. Shen and G. Han, *Journal of Materials Chemistry*, 2012, 22, 20566-20573.
25. T. Zhu, J. S. Chen and X. W. Lou, *The Journal of Physical Chemistry C*, 2011, 115, 9814-9820.
26. M. Y. Son, Y. J. Hong, J.-K. Lee and Y. Chan Kang, *Nanoscale*, 2013, 5, 11592-11597.
27. B. Wang, J. S. Chen, H. B. Wu, Z. Wang and X. W. Lou, *Journal of the American Chemical*

Society, 2011, 133, 17146-17148.

28. B. Wang, H. Wu, L. Yu, R. Xu, T.-T. Lim and X. W. Lou, *Advanced Materials*, 2012, 24, 1111-1116.
29. N. K. Chaudhari, M.-S. Kim, T.-S. Bae and J.-S. Yu, *Electrochimica Acta*, 2013, 114, 60-67.
30. Z. Cao and B. Wei, *Journal of Power Sources*, 2013, 241, 330-340.
31. L. Lang and Z. Xu, *ACS Applied Materials & Interfaces*, 2013.
32. H. Zhang, L. Zhou, O. Noonan, D. J. Martin, A. K. Whittaker and C. Yu, *Advanced Functional Materials*, 2014, 24, 4337-4342.
33. C. Zhu, A. Nobuta, I. Nakatsugawa and T. Akiyama, *International Journal of Hydrogen Energy*, 2013, 38, 13238-13248.
34. C. Zhu, A. Nobuta, G. Saito, I. Nakatsugawa and T. Akiyama, *Advanced Powder Technology*, 2014, 25, 342-347.
35. C. Zhu and T. Akiyama, *Electrochimica Acta*, 2014, 127, 290-298.
36. C. Zhu, A. Nobuta, Y.-W. Ju, T. Ishihara and T. Akiyama, *International Journal of Hydrogen Energy*, 2013, 38, 13419-13426.
37. T. Qiu, J. Wang, Y. Lu and W. Yang, *RSC Advances*, 2014, 4, 23027-23035.
38. C. Wang, G. Shao, Z. Ma, S. Liu, W. Song and J. Song, *Electrochimica Acta*, 2014, 130, 679-688.
39. J. Ye, J. Zhang, F. Wang, Q. Su and G. Du, *Electrochimica Acta*, 2013, 113, 212-217.
40. J. Zhang, T. Huang, Z. Liu and A. Yu, *Electrochemistry Communications*, 2013, 29, 17-20.
41. J.-J. Zhang, Y.-L. Chen, Y.-F. Sun, T. Huang and A.-S. Yu, *RSC Advances*, 2013, 3, 20639-20646.
42. H. Xiao, Y. Xia, W. Zhang, H. Huang, Y. Gan and X. Tao, *Journal of Materials Chemistry A*, 2013, 1, 2307-2312.

Fig 1. Schematic diagram of the experimental setup for solution combustion synthesis (SCS).

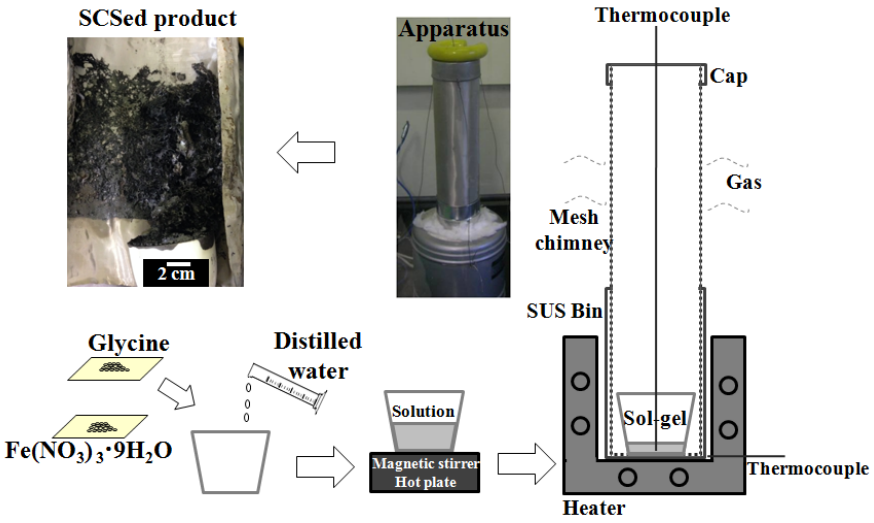

Fig 2. XRD patterns for the samples (a) after SCS, (b) after SCS and heat-treated at 500 ^{o}C for 2 h under Ar, (c) after SCS and heat-treated at 500 ^{o}C for 2 h under air, and (d) after SCS and heat-treated at 600 or 700 ^{o}C for 2 h under Ar.

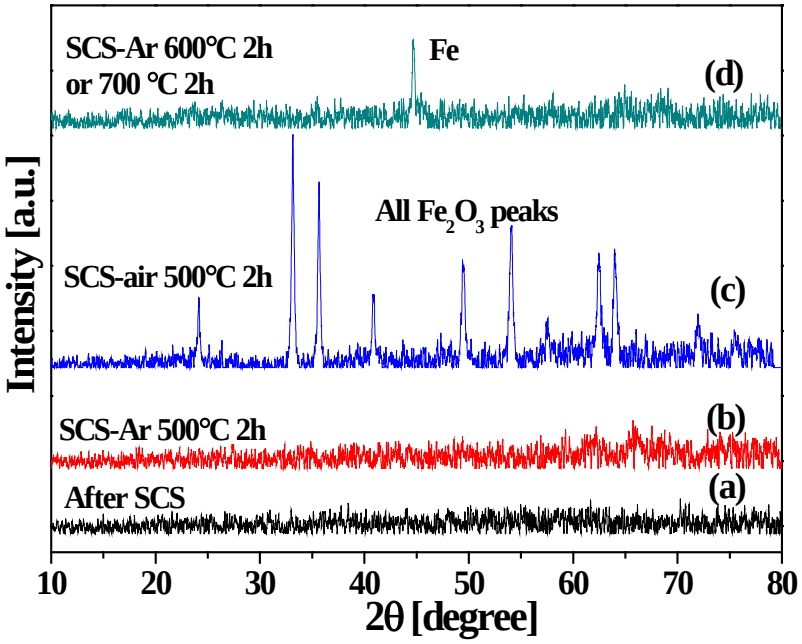

Fig 3. (1) TG curves for samples of: (a) the SCSed precursor under air flow, (b) the SCSed precursor under Ar flow, and (c) the FeO_x/carbon composite under air flow (this sample obtained after SCS and heat-treated at 500 °C for 2 h under Ar).
(2) MS spectra of gases NO and CO_2 during TG analysis of the sample of FeO_x/carbon composite under air flow.

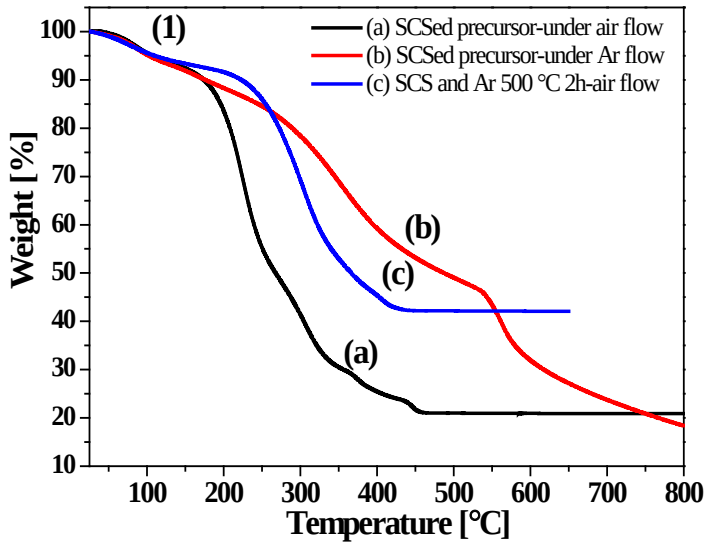

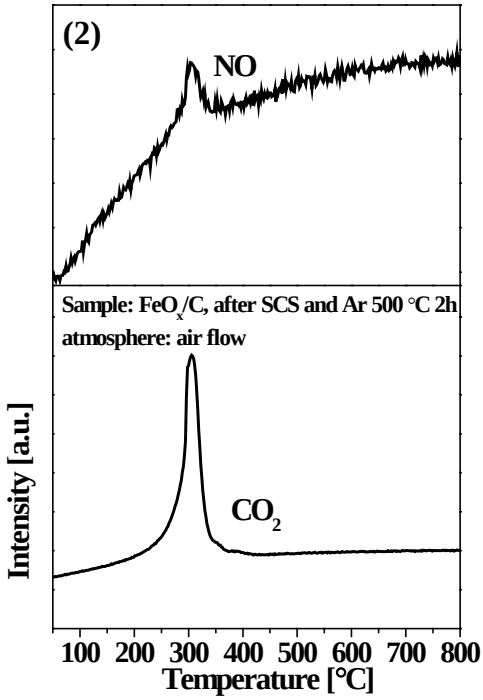

Fig 4. SEM images of the samples (a) FeO_x/C, obtained after SCS and heat-treated at 500 °C for 2 h under Ar, (b) Fe_2O_3, obtained after SCS and heat-treated at 500 °C for 2 h under air. (c) EDS spectra of the FeO_x/carbon composite under SEM observation.

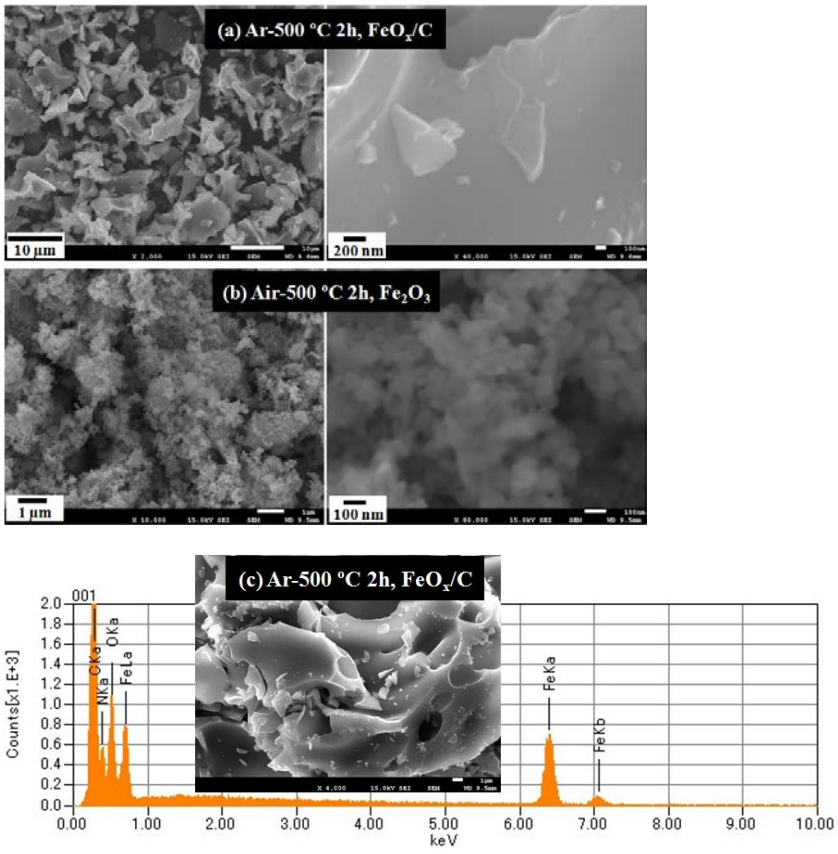

Fig 5. TEM images of the FeO_x/carbon composite.

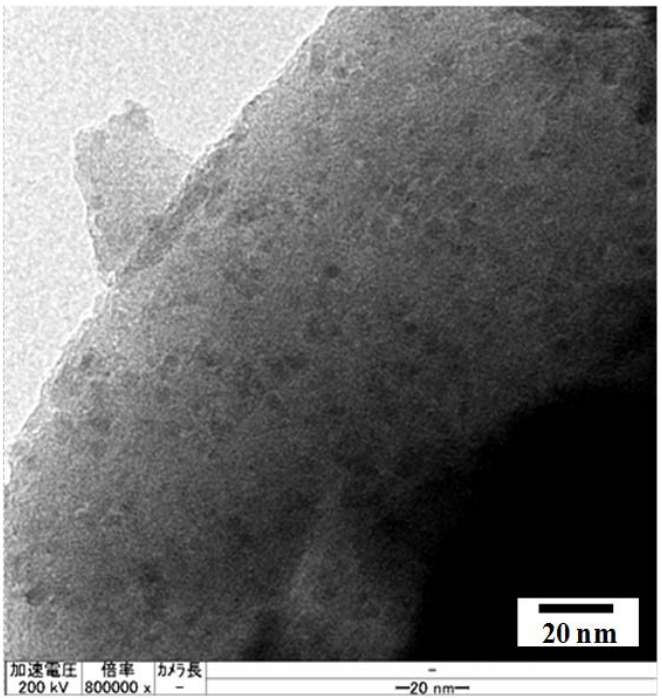

Fig 6. Electrochemical cycling performance of the FeO_x/C composite in comparison with the nanosized Fe_2O_3 at a current density of 500 mA g^{-1}.

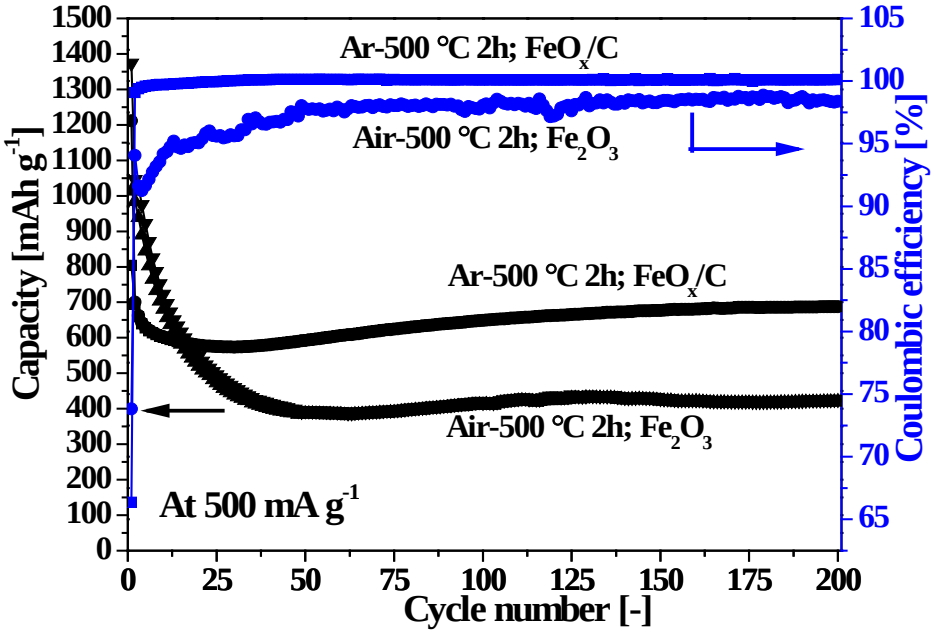

Fig 7. Discharge-charge curves of the FeO_x/C composite and nanosized Fe_2O_3 at a current density of 500 mA g^{-1}.

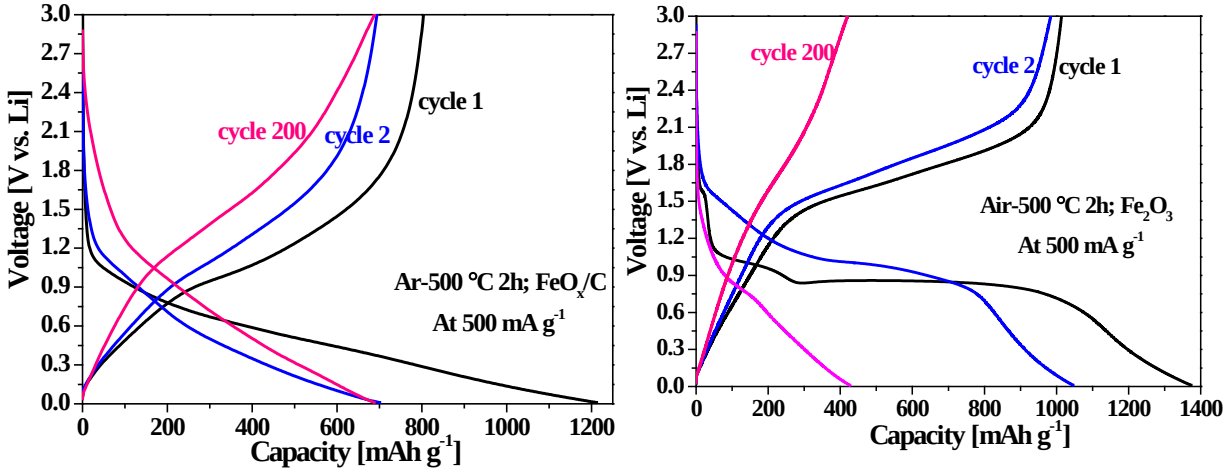

Fig 8. CV curves of the FeO_x/C composite and nanosized Fe_2O_3 at a scan rate of 0.1 mV S^{-1}.

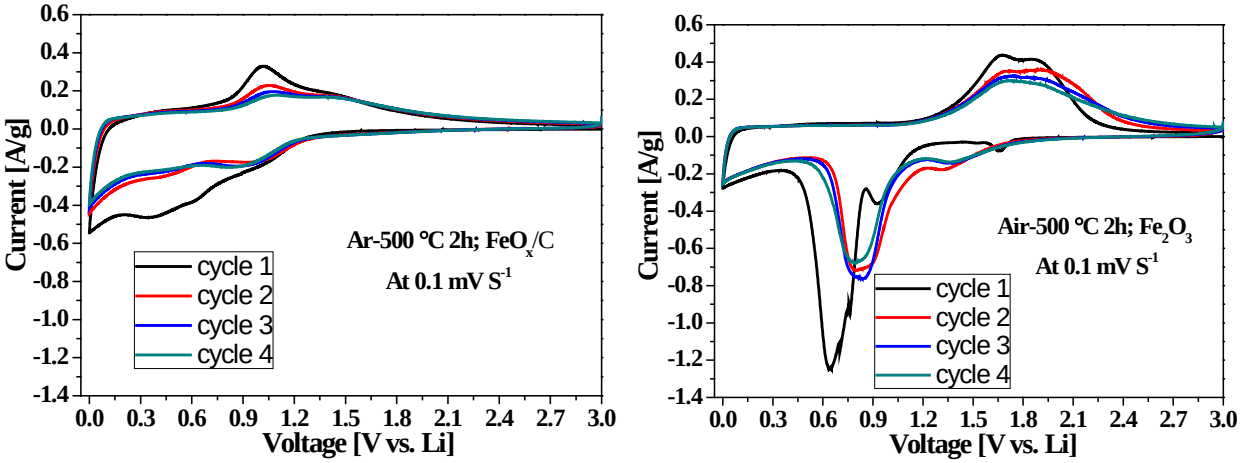

Fig 9. Cycling performance at different current density for the FeO_x/C electrode.

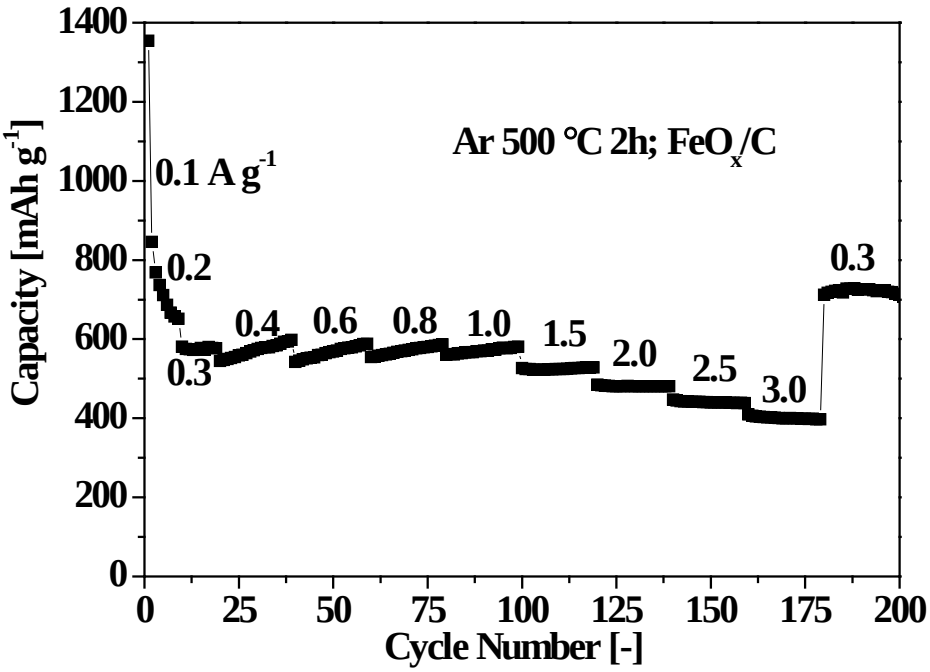
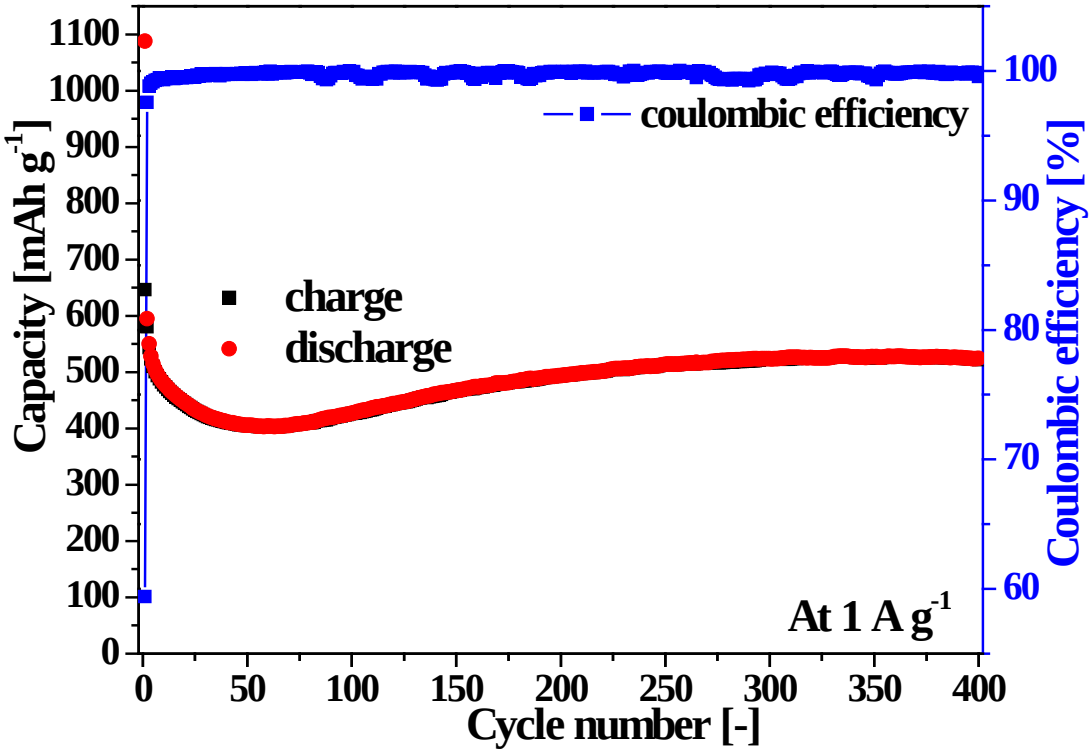
Fig 10. Electrochemical cycling performance of the FeO_x/C composite at a current density of 1 A g^{-1}.